Photon Spectrum Characteristics and Magnetic Field Performance of the Prototype Hybrid Symmetry Undulator Magnet in SRRC

C. S. Hwang[1,2], C. H. Chang[1], F. Y. Lin[1], T. C. Fan[1], Shuting Yeh[1], Ch. Wang[1], P. K. Tseng[1,3], and T. M. Uen[1,2]

[1] *Synchrotron Radiation Research Center, Hsinchu Science-Based Industrial Park, Hsinchu, Taiwan 300, R.O.C.*

[2] *Department of Electrophysics, National Chiao Tung University, Hsinchu, Taiwan 300, R.O.C.*

[3] *Department of Physics, Tamkang University, Tamsui, Taiwan 251, R.O.C.*

(Received April 29, 1997)

A prototype Halbach hybrid magnet structure undulator with period of 10 cm was used to achieve a high magnetic field. A nearly sinusoidal magnetic field strength of 0.964 Tesla at 24 mm gap was achieved. The magnetic field was also designed and calculated using the magneto-static 3-D code of "TOSCA". According to those results, the field uniformity was better than 0.1% in the field rolloff range of $x = \pm 10$ mm at 24 mm gap. The real field profile was measured to find the magnetic field behavior and the photon energy spectrum characteristics. In addition, field distributions obtained from the field measurement and simulation were used to calculate the photon spectrum characteristic. After the multipole and spectrum shimming, the good field region was controlled within 100 G·cm in the range of -2 cm $\leq x \leq$ 2 cm to increase the dynamic aperture. A maximum phase error around 5.5 degrees was achieved and then maintained a high flux in the higher harmonic spectrum. The photon flux intensity is very close to the value of the ideal field simulation, which is about 10^{15} photons/sec/100mA/0.1%BW. The energy range of the first harmonic ranges from 5.2 to 220 eV and the higher harmonic energy can reach 1 KeV. The electron trajectory deviation was controlled to within 5 μm to maintain a constant optical axis and satisfy the beam dynamic requirements.

PACS. 01.52.+r – National and international laboratory facilities
PACS. 07.55.Db – Generation of magnetic fields; magnets.

I. Introduction

To study the atomic and molecular spectroscopy in photochemistry, photophysics, and chemical reaction dynamics, a high photon flux source in the range of 5.2 - 100 eV is necessary. The high photon flux source will enhance the resolution of the data analysis and increase reliability. Therefore, a prototype C-type hybrid undulator with a period of 10 cm (U10P)[1-2] was designed and constructed to obtain the high flux. The undulator will produce the first. harmonic photon energy in the range of 5.2 to 220 eV on the 1.5 GeV storage ring. The higher harmonic energy range of 50 - 1000 KeV can also be achieved for the other users. This undulator can obtain a higher photon flux several hundred times

larger than the bending magnet. This tendency occurs because the photons emitted from each pole are coherent with each other. The photon flux intensity for the U10P with twenty periods has reached 10^{15} photons/sec/100mA/0.1%BW. This undulator has been installed in a 1.5 GeV storage ring of the Synchrotron Radiation Research Center (SRRC).

The U10 undulator is a 20 period device having a period length of 10 cm, capable of providing a nearly sinusoidal magnetic field strength of 0.964 Tesla at the magnet gap of 24 mm. A Halbach type hybrid structure magnet was designed to achieve a high field strength at a given ratio of magnet gap to period (2.4/10). Figure 1 schematically depicts the magnetic structure of U10P.

The magnetic field measurement was performed by the 3-D Hall probe [3] and a long loop coil measurement system [4]. The 3-D Hall probe was also used to measure the field distribution of vertical field B_y, horizontal field B_x, and longitudinal field B_z. Depending on the field distribution, the electron trajectory can be determined and the spectrum analyzed as well. For a rapid integral field measurement, a long loop coil was used to measure the transverse components of the vertical field $\int B_y ds$ and the horizontal field $\int B_x ds$. Depending on the field measurement results taken by the Hall probe and the long loop coil, the multipole field distribution (homogeneity of the integral field strength in the transverse axis) can be obtained. After the shimming [5-7] (the multipole shimming), the multipole field strength can be controlled within the specification. To maintain a high spectrum flux intensity, the electron phase should be modified with the shimming technique (the spectrum shimming) [5-7]. This modification depends on the Hall probe mapping results. After the shimming technique, the good field region was controlled to 100 G·cm in the range of-2 cm $\leq x \leq$ 2 cm to increase the dynamic aperture. Meanwhile, the 1000 eV of the photon energy can be obtained.

The photon energy was created from U10P corresponds to the main energy range of 5.2 to 100 KeV. When the field strength was altered by opening the gap, it will provide a higher harmonic energy within the energy range of 50 to 1000 eV. After the spectrum shimming, the phase error was controlled at 1 to 5.5 degrees across the whole magnet gap. The first harmonic ratio can keep within 90% between the real field of the Hall probe measurement and the ideal field of the simulation. At a twenty-first harmonic spectrum, the photon flux intensity ratio is still within 60%.

II. Magnet design and configuration

The magnet is a Halbach type with the hybrid structure. The pole material is a vanadium permendur (8.4 x 1.6 x 6.2 cm^3) and the magnet is the permanent magnet blocks NeFeB (3.8 x 3.8 x 3.4 cm^3). The magnet has an average magnetization of 1.22 Tesla and an intrinsic coercive force of 11.0 Koe. Fig. 1 displays the magnet array structure and Table I lists the design parameters. The dipole moment variation and the disorientation error of the U10P are set to be less than 1% and 2 degrees, respectively. This specification of magnet block will still create a smaller field strength deviation and the multipole field components; however, it will be reduced as small as possible by sorting the magnet blocks. The magnet blocks were sorted according to the sum of M_x^2 and M_y^2 to optimize the field strength of each pole. Where M_x and M_y denote the dipole moments of each block and can be measured by the Helmholtz coil measurement system [8]. The mechanical structure

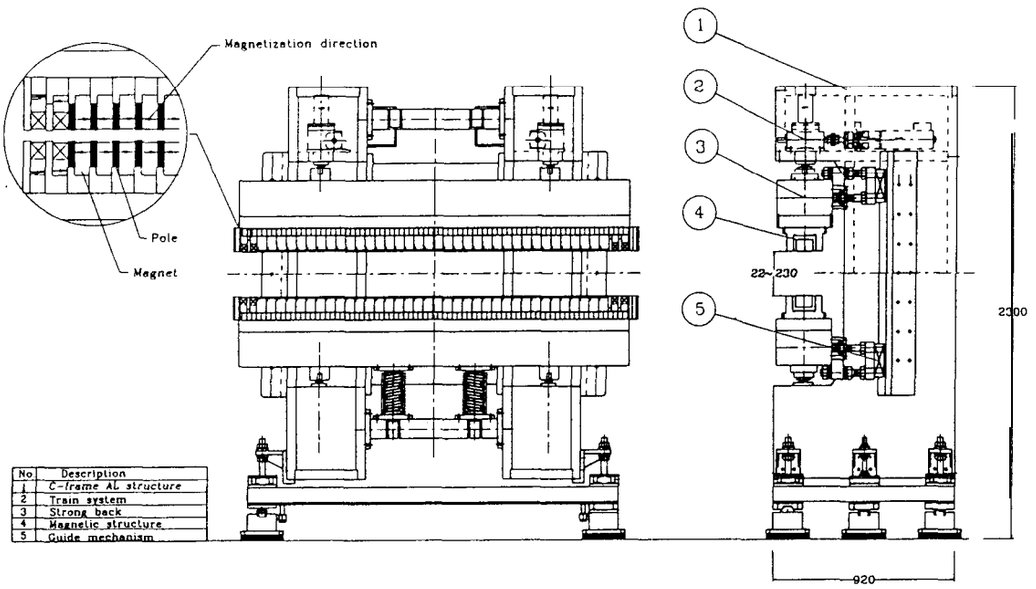

FIG. 1. The schematic view of the mechanical structure design of U10P.

TABLE I. Main design parameters of the hybrid U10P undulator.

Period length (cm)	Period number	Gap range (mm)	Effective field (@ 24 mm gap)	Rolloff (@$x = \pm 1$ cm)	Field uniformity ($(\Delta B/B)$rms)
10	20	22-230	> 0.945 T	< 0.1%	< 0.5%

consisted of two C-frame supports and two strong backing beams. Stress analysis was also performed using a 3-D code "ANSYS". The mechanical structure consists of a drive system, including four independent brushless servo motors, gears, torque limiters and an optical linear encoder system. Gap reproducibility in one direction (in out-bound or in-bound) is better than 12 μm. Hard stops prevent the vacuum chamber from damage in case of an accident. Figure 1 schematically depicts the mechanical design structure of U10P. Table II presents the beam dynamic and photon spectrum requirements on magnetic performance.

III. Magnetic field measurement and field performance

Magnetic shimming generally consists of placing small pieces of ferromagnetic material

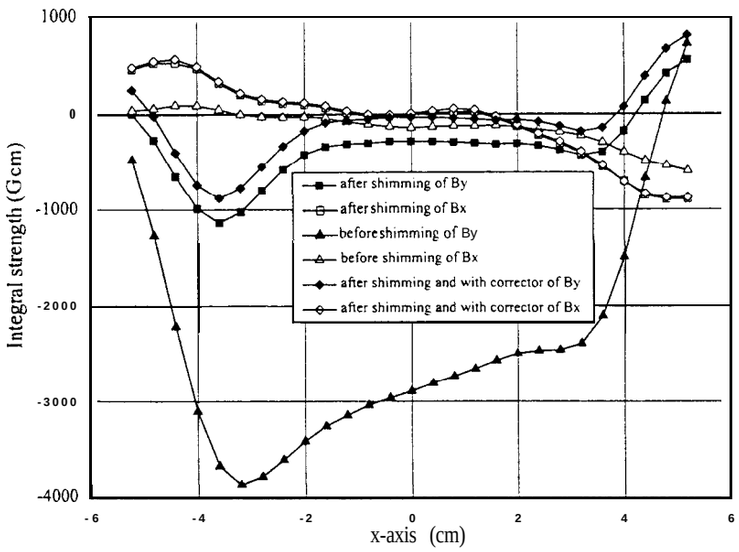

FIG. 2. Integral field strength distribution of the vertical and horizontal transverse field as a function of transverse axis under before shimming, after shimming, and after shimming with the excitating end vertical field corrector. (a) Vertical multipole field distribution, (b) Horizontal transverse multipole field distribution.

on the pole or magnets of an undulator to make local corrections to optimize the electron trajectory and the photon behavior [5-6]. The shim effectively shunts some of the flux of the magnet and the effect resembles a reduction of the magnetic magnetization. Therefore, shimming techniques can correct the transverse variation of field integrals for multipole field and trajectory correction to improve the dynamic aperture. The shimming technique reduces the deviation of the peak field of each pole and half period integral field to obtain a coherent light source to increase the spectrum flux.

For the multipole field correction, the magnetic field measurement results with and without shim are shown in Fig. 2. After shimming, the good field region is wider than previously. In Fig. 2, the first integral field strength on-axis has been reduced to 200 G·cm after adding the shims in the magnet. The residual first integral field strength can be reduced to zero by the two end coil corrector. The first integral strength was used to determine the electron angle distribution and the second integral strength was used to decide the electron trajectory distribution. Definitions of the first $I_1(z')$ and second $I_2(z'')$ integrals of the vertical and horizontal magnetic field components are provided as

$$I_{1,p}(z' = \infty) \equiv \int_{-\infty}^{z'} B_p(z)dz, \qquad p = x, y, z, \tag{1}$$

$$I_{2,p}(z'' = \infty) \equiv \int_{-\infty}^{z''} dz' \int_{-\infty}^{z'} B_p(z)dz, \quad p = x, y, z. \tag{2}$$

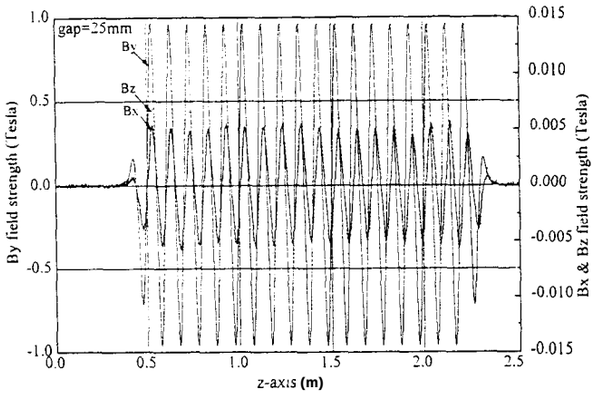

FIG. 3. Peak field distribution of B_y , B_x and B_z along the longitudinal axis has been presented. The peak field strength occurs at the same position on the longitudinal axis.

Where $I_{1,p}$, $I_{2,p}$, and B_p denote the three field component of the first and second integral field strength as well as the peak field strength with p = x, y, z. Two active coil correctors located at the two ends of the UlOP. The up-stream coil corrector is used to correct the second integral (electron trajectory) and the down-stream coil is for the first integral (electron angle) correction. After the two coil correctors have been excited, the multipole field distribution on-axis is revealed, as indicated in Fig. 2. This finding suggests that the first integral strength on-axis has been within 100 G·cm. Meanwhile, Fig. 3 displays the field distribution of the three components of B_y, B_x, and B_z along the longitudinal axis. According to this figure, the peak fields of B_x and B_z (about 50 Gauss) are so small, that they can not influence the electron and photon beam behavior. The electron trajectories can be calculated by the three magnetic field strength distributions (Fig. 3) and shown in Fig. 4. The trajectories R_x, R_y, and the trajectory angle θ_x, θ_y of the electron orbit are calculated by Eq. (3) though (6).

$$R_x(z'') = \frac{I_{2,y}(z'')}{B\rho} + \frac{I_{2,z}(z'') \cdot \theta_y(z')}{B\rho}, \tag{3}$$

$$R_y(z'') = \frac{I_{2,x}(z'')}{B\rho} + \frac{I_{2,z}(z'') \cdot \theta_x(z')}{B\rho}, \tag{4}$$

and

$$\theta_x(z') = \frac{I_{1,y}(z')}{B\rho}, \tag{5}$$

$$\theta_y(z') = \frac{I_{1,x}(z')}{B\rho}, \tag{6}$$

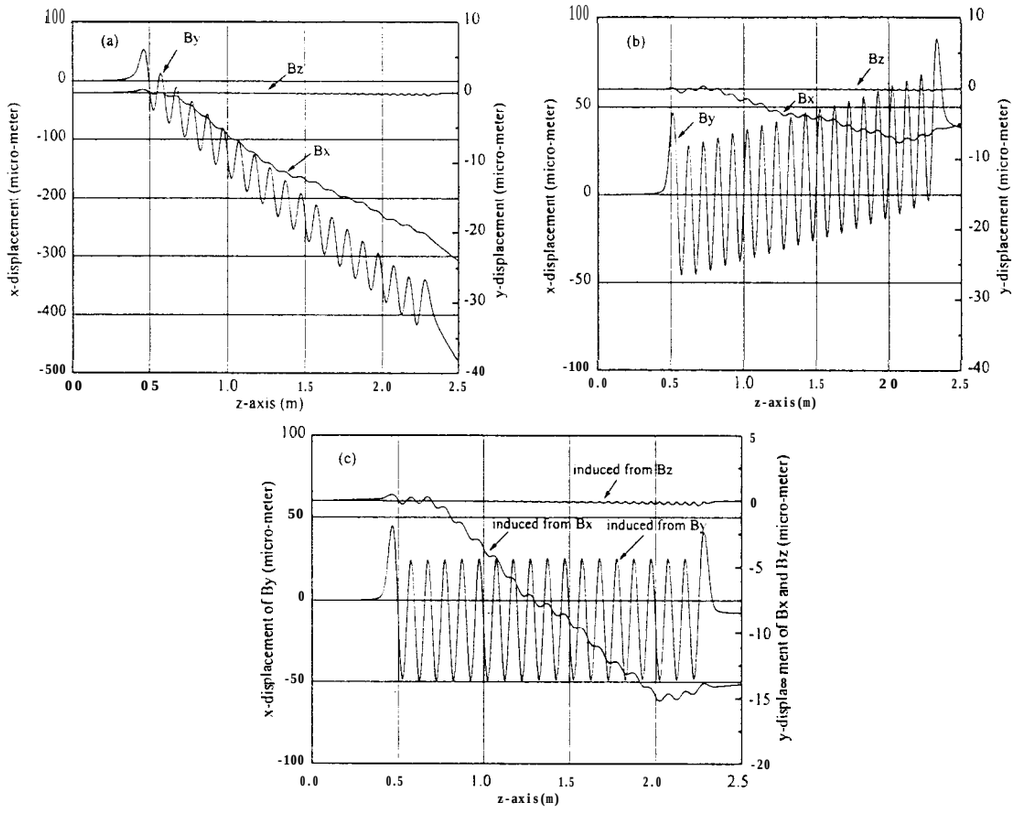

FIG. 4. Electron trajectory deviation on the vertical and horizontal transverse axis which induces from the vertical, transverse and longitudinal field distribution. (a) Before shimming, (b) After shimming, (c) After shimming and with excitating the vertical field corrector.

Where $B\rho$ = 5.003 T·m denotes the rigidity of the 1.5 GeV storage ring. Because the angle $\theta_y(z')$ and $I_{2z}(z'')$ in the second term of Eqs. (3) and (4) are too small, the trajectory R_x coming from the longitudinal field can be neglected. The average electron trajectories of $\overline{R_x}(z)$ and $\overline{R_y}(z)$ should be straight within $\pm 20\,\mu$m and the average trajectory angle $\overline{\theta_x(z)}$ and $\overline{\theta_y}(z)$ of trajectory should be within $\pm 40\,\mu$rad. The average trajectory and the trajectory angle of the electron orbit can be calculated by Eqs. (7) and (8).

$$\overline{R_p}(z) = \frac{1}{2}\left(R\left(z - \frac{\lambda u}{4}\right) + R\left(z + \frac{\lambda u}{4}\right)\right), \qquad p = x, y, \tag{7}$$

$$\overline{\theta_p}(z) = \frac{1}{2}\left(\theta\left(z - \frac{\lambda u}{4}\right) + \theta\left(z + \frac{\lambda u}{4}\right)\right), \qquad p = x, y, \tag{8}$$

where λ_u denotes the periodic length of the U10P undulator. Fig. 4 shows the electron

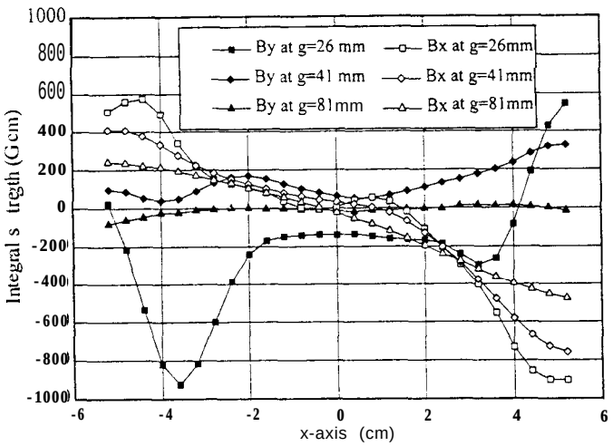

FIG. 5. The multipole field behavior as a function of different gaps. The higher multipole field strength and the dipole integral strength are all changed when the gap changes. Although the dipole integral strength has changed 200 G·cm, it can be corrected by the end pole corrector.

trajectory distribution before and after shimming as well as after shimming with the excitation corrector. Fig. 4(c) indicates the trajectory deviation is within 5 μm, but the exit beam has a 10 μm offset which indicates the electron beam has been shifted 10 μm in the exit location of the U10P undulator. This offset is so small that it will be easily corrected by the corrector and will not influence the close orbit or the spectrum quality. Figure 4 also reveals that a small kicker (about 0.01 mrad) appears on the vertical axis which is induced from the B_x field at $z = 0.71$ m. This kicker originates from the third period which has a significantly higher negative integral strength than the positive one. The amount of kicker is small, thereby making it easy to correct this by the vertical correctors. However, the shim technique can still correct the vertical kicker.

Although the multipole field has been reduced to obtain a wide good field region, the gap opening will create a strong multipole field strength and subsequently reduce the good field region. As Fig. 5 indicates, the dipole integral strength has also changed. The integral field strength can be expanded as Eq. (9) to obtain the normal and skew multipole components.

$$\int_{-\infty}^{\infty} (B_x + iB_y)dz \cong \sum_{n=0}^{n} (b_n + ia_n)(x + iy)^n. \tag{9}$$

Where a, and b_n denote the integral normal and skew components. Figure 5 reveals that the integral strength of the dipole and the higher multipole field are changed as a function of gap. This change occurs because differential magnetization has also occurred on the different pole. Since this undulator magnet is a symmetric structure, the magnetization field of the two end poles (the fringe field strength depends on the gap) located at the two

TABLE II. Specification requirement of electron and photon performance of the U10P undualtor in the good field range of $x = \pm 1$ cm for whole magnet gap.

Beam dynanic							Spectrum		
$I_{1,y}$ & $I_{1,x}$ (G·cm)	$I_{2,y}$ & $I_{2,x}$ (G·cm^2)	a_1 & b_1 (G)	a_2 & b_2 (G/cm)	a_3 & b_3 (G/cm^2)	$\Delta B_p/B_p$ $(\Delta B_{I_p}/B_{I_p})$	slope η (m^{-1})	$\Delta R_{x,y}$ (μm)	$\Delta\theta_{x,y}$ (wad)
[100]	[50000]	[100]	[100]	[100]	[0.5%]	[10^{-4}]	[20]	[40]
(50) (60)	(5000)(6700)	(31)(64)	(26)(50)	**(8) (42)**	**(0.1%)**	**(8 x 10^{-6})**	(5)	**(30)**

() presents the maximum value of field measurement results for the gap change from **24** mm to **220** mm and [] presents the specification values.

sides of the undulator. This is in contrast to the central poles such that the dipole integral strength will be changed at a different gap. Magnetic field measurement and analysis results of the U10P undulator verify that a hybrid structure undulator can be designed with an antisymmetric structure that the systematic multipoles in the end fields will tend to automatically cancel each other, leaving only the random components to be corrected. The end section at the entrance and exit of the undulator are identical, and the distance between the end pole and magnet blocks are tunable, then the integral strength will be independent of the gap. This method is called the passive correction skill. If magnet poles are designed at a minimization of pole saturation and demagnetizing fields on magnet by using sufficient magnet overhangs to reduce flux leakage, then the multipole field deviation at different gaps would be reduced as small as possible. Therefore, the second integral strength can be hold constant and close to be zero. However, if the multipole field strength can keep within the specification, the end coil corrector can be used to compensate for the first integral field strength close to zero. Such a compensation is called the active correction skill. After the field measurement and analysis results, the multipole strength and trajectory all fulfill specifications. Table II compares the specification requirements and the experiments.

IV. Photon spectrum characteristics and performance

The radiation spectrum of the critical energy of a bending magnet is around ε_c. Where $\varepsilon_c(KeV) = 0.665E^2(GeV)$ ***B(T).*** For the insertion device, wigglers can be regarded as a sequence of bending magnets of alternating polarity. Hence, the radiation features are similar to those from bending magnets. However, the intensity will be enhanced 2N times of the bending magnet. Where N denotes the periodic numbers of insertion device. In undulators, the interference of the radiation spectrum from different poles will be enhanced N^2 times of the bending magnet. Eq. (18) describes the radiation harmonic energy E_n. Meanwhile, the relative bandwidth at the nth harmonic spectrum is

$$\frac{\mathrm{Aw}}{\mathrm{W}}\mathrm{M} \quad \frac{1}{nN}. \tag{10}$$

To maintain the photon spectrum quality of the magnetic field measurement as good as the ideal magnetic field simulation, the deviation of $\Delta B_p/B_p$ between each pole peak field strength and the deviation of $\Delta I_{1/2}/I_{1/2}$ between the half period integral strength should be maintained within 0.5%. The deviation calculation of $\Delta B_p/B_p$, and $\Delta I_{1/2}/I_{1/2}$ are

$$\frac{\Delta B_p}{B_p} \equiv \frac{\sqrt{\sum_{i=1}^{i=N_p} (|B_{peak}| - \langle |B_{peak}| \rangle)^2 / N_p}}{\langle |B_{peak}| \rangle}, \tag{11}$$

$$\frac{\Delta I_{1/2}}{I_{1/2}} \equiv \frac{\sqrt{\sum_{i=1}^{i=N_p} (|I_{1/2}(period/2)| - \langle |I_{1/2}(period/2)| \rangle)^2 / N_p}}{\langle |I_{1/2}(period/2)| \rangle}, \tag{12}$$

where

$$\langle |B_{peak}| \rangle = \frac{1}{N_{rp}} \sum_{i=1}^{i=N_p} |B_{peak}|. \tag{13}$$

$$\langle |I_{1/2}(period/2)| \rangle = \frac{1}{N_{rp}} \sum_{i=1}^{i=N_p} |I_{1/2}(period/2)|. \tag{14}$$

Where B_{peak} and $I_{1/2}(\mathrm{period}/2)$ denote the peak field strength and the half period integral field strength. These two factors determine the phase error $\Delta\phi_{rms}$[7,9-11] which, subsequently, determine the radiation spectrum quality. The phase error $\Delta\phi_{rms}$ correlates with the radiation phase $\phi(t)$ in Eq. (16). The photon construction or destruction will rely on the energy radiation phase $\phi(t)$, thereby constraining the energy radiation of the photon flux distribution in Eq. (15) [7,9-11].

$$\frac{d^2\Psi}{d\omega d\Omega} = \frac{e^2\omega^2 Z_0}{16\pi^3} \left(\int_{-\infty}^{\infty} n \times (n \times \beta) e^{i\omega\phi(t)} dt \right)^2, \tag{15}$$

$$\phi(t) = \omega \left(t - \frac{\boldsymbol{n} \bullet r(t)}{c} \right) \tag{16}$$

Where e denotes the electronic charge, Z_0, represents the impedance of free space, n is the unit vector, $\beta = \nu/c$ and $r(t)$ are the electron velocity and position vector. On-axis, the radiation phase and radiation energy of the relativistic electron depends on the deviation of the half integral strength $\Delta I_{1/2}/I_{1/2}$ and the deviation of peak field strength $\Delta B_p/B_p$ at each poles location. Therefore, depending on Eq. (11) to (14), the values of $\Delta B_p/B_p$ and $\Delta I_{1/2}/I_{1/2}$, indicated in Table II, can be compared with the specification requirements. The slope η should be less than $10^{-4}/\mathrm{m}$. This is obtained from the absolute values of the peak field strength of the magnetic poles excluding the end correctors. The slope is least-square fitted to a straight line as

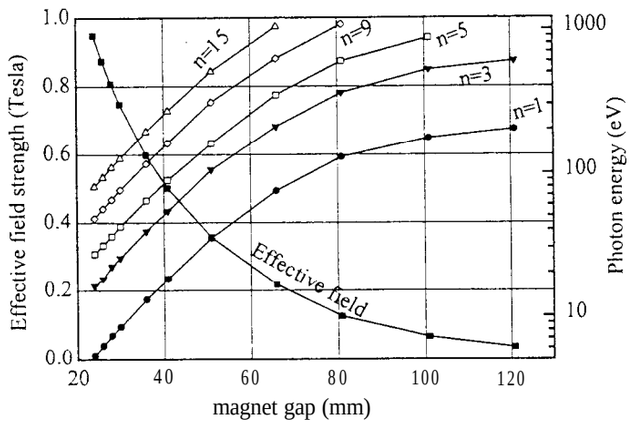

FIG. 6. Effective magnetic field strength B_{eff} and the harmonic spectrum energy distribution as a function of gap are presented. This result shows the usable energy range in the U10P undulator magnet.

$$|B_{peak}(z)| = B_0(1 + \eta z). \tag{17}$$

Above constraining condition η can control the magnet without taper. This taper will destroy the spectrum quality and is indicated in Table II.

Effective magnetic field strength B_{eff} as a function of gap has been measured and Fig. 6 reveals that B_{eff} decreases exponentially. This effective field strength B_{eff} determines the photon emission energy E_n, which can be calculated by Eq. (18) and expressed as

$$E_n(KeV) = \frac{n \cdot 0.95 E_e^2(GeV)}{\lambda_u(\mathrm{cm})(1 + K^2/2 + \gamma^2\theta^2)}. \tag{18}$$

Where n denotes the odd harmonic spectrum numbers, θ denotes the angle between the electron source and the observer, $E_e = \gamma mc^2$ represents the relative energy of the electrons, and K = 0.934 $B_{eff}\lambda_u, \lambda_u$ is the periodic length. The photon energies of each harmonic can be calculated by Eq. (18) and are shown in Fig. 6. Effective magnetic field strength B_{eff} can be obtained by means of Eq. (19) to fit the measurement field strength distribution of $B_y(z)$.

$$B_y(x = y = 0, z) \cong \sum_{n=1}^{n=odd} B_n \cos\left(\frac{2n\pi z}{\lambda_u} + \phi_n\right). \tag{19}$$

and

$$B_{eff} = \sqrt{\sum_{n=1}^{n=odd} \left(\frac{B_n}{n}\right)^2}. \tag{20}$$

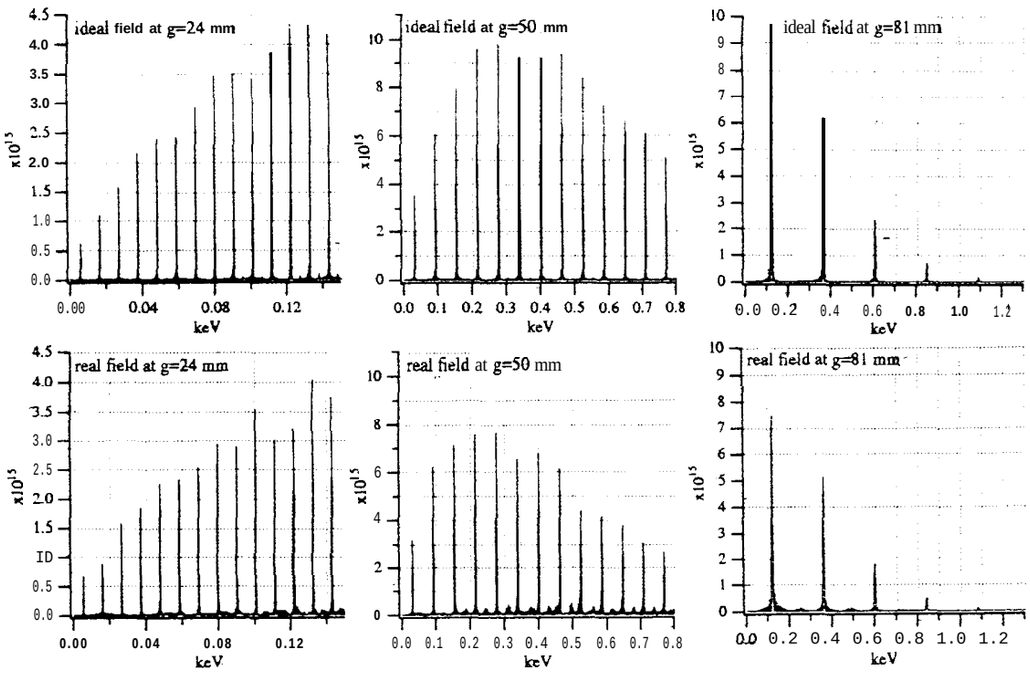

FIG. 7. Harmonic spectrum flux of the real field measurement and the ideal field simulation has been calculated at different magnet gaps of 24 mm, 50 mm and 81 mm.

Fig. 6 indicates that the photon energy can be used in the range of 5.2 to 1100 eV of the U10P undulator.

The harmonic spectrum flux distribution of the real field measurement and ideal field simulation at 24 mm (k=8.87, and B_{eff}=0.95 T), 50 mm (k=3.33, and B_{eff}=0.357 T) and 81 mm (k=0.98, and B_{eff}=0.105 T) magnet gap are shown in Fig. 7. When $k >> 1$, the spectrum flux will increase when the spectrum harmonic number is increased; however it will decrease when distant from the first harmonic. If $k \geq 1$, then the spectrum flux intensity increases and then decreases symmetrically while increasing the spectrum harmonic. If $k \leq 1$ then the flux intensity will decrease rapidly when increasing the spectrum harmonic numbers. Figure 8 presents the harmonic spectrum flux intensity and the flux ratio between the filed measurement and the ideal field simulation as a function of harmonic number at four gap. Some harmonic flux of the real field is bigger than the ideal field and some harmonic flux of the real field is less than the ideal field. This is because the real end pole fields will construct or destroy each other. These interference fields will contribute the different photon intensity on some harmonic spectrum, even after the spectrum shimming. Figure 8 also reveals that the real and ideal first harmonic spectrum ratio at small gap is bigger than 100%, but the ratio will reduce to be 90% at the higher harmonic spectrum. This is because the number of full strength poles at small gaps exceeds the number of gap-independent full strength poles. The higher harmonic spectrum flux ratio decreases

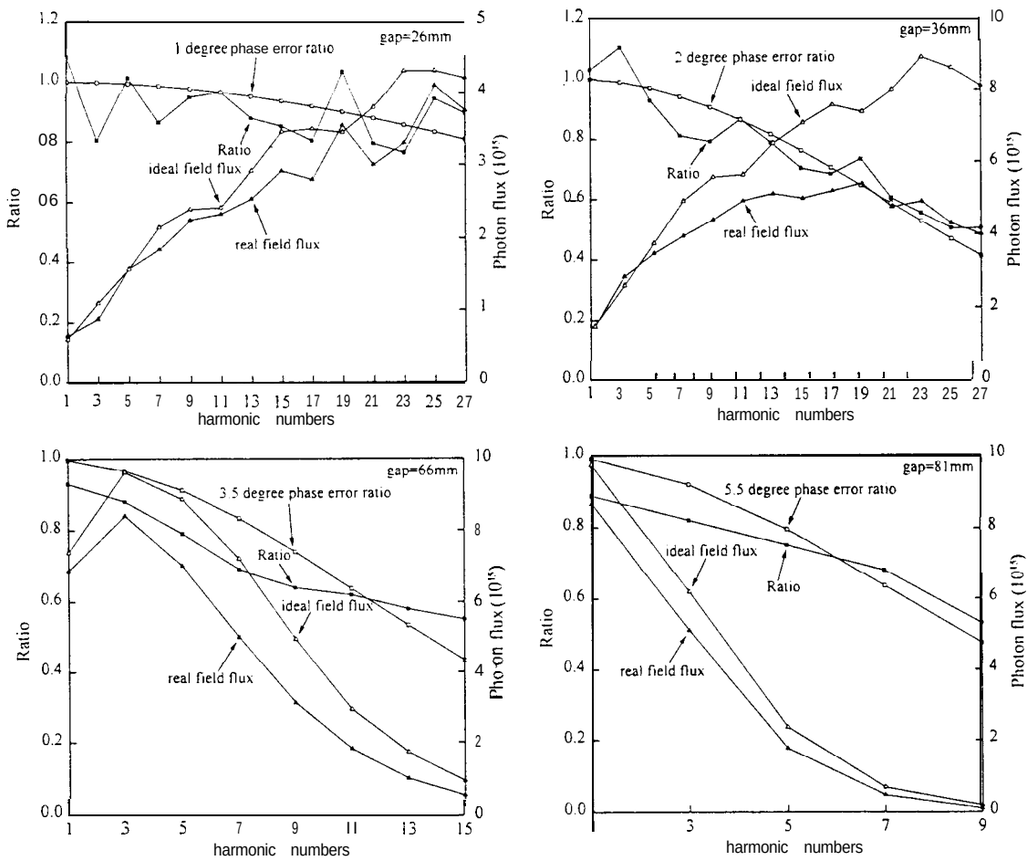

FIG. 8. The photon flux intensity of each harmonic spectrum and the flux ratio between the ideal and real field calculation has been presented at four magnet gaps. The flux ratio has been compared with the phase error prediction (photon flux unit is photons/sec/100mA/0.1%BW).

more dramatically than the lower harmonic spectrum. This is because the magnet field is not perfect and phase error $\Delta\phi_{rms}$, will be created. Kotably, a correlation arises between the flux intensity I and the rms phase error $\Delta\phi_{rms}$. Eq. (21) shows the empirical formula between spectrum flux and phase error. The correlation can be realized from the prediction in Fig. 8.

$$I = I_0 e^{-(n\Delta\phi_{rms})^2}. \tag{21}$$

Where I and I_0 represent the spectrum flux densities with and without phase error. Figure 8 also indicates the intensity ratio between the phase error prediction and the real field

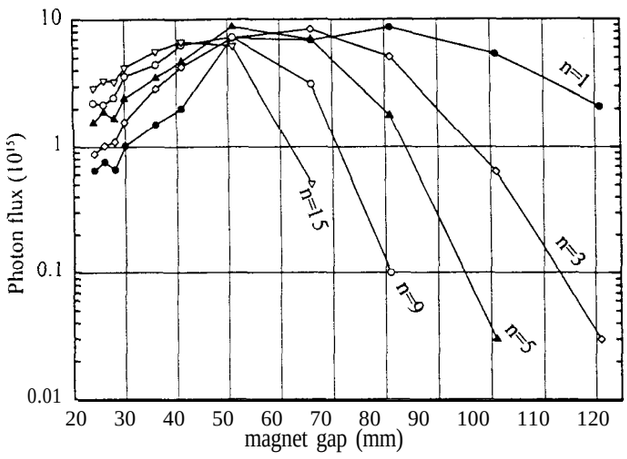

FIG. 9. The harmonic spectrum flux intensity as a function of different gaps of the real field calculation is presented here. The maximum flux intensity will be shifted to the lower magnet gap to increase the harmonic number (photon flux unit it photons/sec/100mA/0.1%BW).

spectrum normalization. Hence, the phase error changes from 1° to 5.5" at different gaps. Figure 9 illustrates the relationship between the usable energy range and the photon flux intensity. Above result shows that the maximum flux intensity will be shifted to the lower magnet gap (strong peak field strength region) when the harmonic number is increased. These results can support a design criteria for the undulator magnet. Figure 6 and 9 demonstrate that the usable photon energy range of the U10P is about 5.2 to 1100 eV. In this range, the photon flux remains above 0.5 x 10^{15} photons/sec/100mA/0.1%BW.

V. Conclusion

Experiments involving the shimming technique suggest that the multipole shim should be done before the spectrum shim, because the spectrum shimming does not change the multipole components. If the integral multipole field strength and the first integral strength on-axis are held constant while the gap changes, then the antisymmetric structure magnet and the passive end pole with a distance tunable design are necessary. Also, the design concept for minimizing pole saturation and demagnetizing fields of magnet using sufficient magnet overhangs to reduce flux leakage is necessary.

The relationship between the photon energy and the photon flux in different harmonic spectrum (compare with Fig. (8) and (9)) can be used as the criteria to design the usable energy range of the undulator magnet. Based on the spectrum shimming technique, the flux intensity of the higher harmonic spectrum (about *30th* harmonic spectrum) should also be maintained at a high flux ratio (larger than 40%) if the phase error can be modified to within 2 degrees. Hence, a undulator can be designed for use at the low energy of VUV range (in lower harmonic spectrum) and the high energy x-ray range (in higher harmonic

spectrum). Moreover, measurement and analysis results confirm that the end pole also contributes a considerable quantity components for the harmonic spectrum in such a 20 periods undulator with a 10 cm periodic length. Finally, after the multipole and spectrum shimming, the undulator performance fulfills the specifications.

This U10P has been installed in the storage ring. The testing has verified that the electron beam does not obviously change under the dynamic tuning for different energy scans. However, no extra beam lines are available to measure the photon spectra. Therefore, a new and flexible beam line with a monochromator will hopefully be completed within one year to measure the photon spectra for different kinds of insertion device. This beam line can also measure the absolute photon intensity.

Acknowledgements

The authors are indebted to Dr. Pascal Elleume (ESRF) for valuable discussions regarding the field analysis and his useful B2E spectrum analysis code. We would like to thank the Director Y.C. Liu, Deputy Director (SRRC), C. T. Chen (SRRC), and Dr. J. R. Chen (SRRC) to support this project. SRRC staff members of J. Y. Hsu, H. H. Chen, K. H. Chen are also commended for their technical assistance.

References

[1] C. H. Chang, L. H. Chang, H. H. Chen, T. C. Fan, C. S. Hwang, D. L. Kuo, J. Y. Hsu, F. Y. Lin, Ch. Wang, Shuting Yeh, IEEE Trans. on Magn. 32, 2629 (1996).

[2] C. H. Chang *et al.*, Technique Manual of *the U10P/SRRC,Undulator Magnet* (A technical report of SRRC, Hsin-chu, January 1996).

[3] C. S. Hwang, T. C. Fan, F. Y. Lin, Shuting Yeh, C. C. Chen C. H. Chang, SRRC/MG/IM/97-01 (1997).

[4] C. S. Hwang, T. C. Fan, F. Y. Lin, Shuting Yeh, C. C. Chen, C. H. Chang, SRRC/MG/IM/97-01 (1997).

[5] Bruno Diviacco, Richard P. Walker, Nucl Instr. and Meth. A368, 522 (1996).

[6] J. Chavanne *et al.*, ESRF Internal Report SR/ID-89-27 (1989).

[7] J. Chavanne *et al.*, ESRF Internal Report SR/ID-89-32 (1989).

[8] C. S. Hwang, Shuging Yeh, P. K. Tseng, T. M. Uen, Rev. Sci. Instrum. 67, 1741 (1996).

[9] B. L. Bobbs, G. Rakowsky, P. Kennedy, R. A. Cover, and D. Slater, Nucl. Instr. and Meth. A296, 574 (1990).

[10] Roger J. Dejus, Isaac Vasserman, Elizabeth R. Moog, and Efim Gluskin, Rev. Sci. Instrum. 66, 1875 (1995).

[11] B. M. Kincaid, J. Opt. Soc. Am. B2, 1294 (1985).